Frontiers in Computing and Intelligent Systems
ISSN: 2832-6024 | Vol. 12, No. 1, 2025

Algorithm of Non-LTE Infrared Radiation in Atmosphere and Its Application

Jian Wang [1, 2], Shuaihui Li [1, 2, a], Dandan Zeng [1, b], Bo Yan [1, 2], Hao Chen [1]

[1] State Key Laboratory of High Temperature Gas Dynamics, Institute of Mechanics, CAS, Beijing 100190, China
[2] School of Engineering Science, University of Chinese Academy Sciences, Beijing 100190, China
[a] lee@imech.ac.cn, [b] zengdadan@imech.ac.cn

Abstract: Atmospheric radiation is widely used in the field of space-based detection of spacecraft and atmospheric remote sensing. With the increase of altitude, the air density decreases and the intermolecular collision becomes weaker. As a result, the energy distribution of gas molecules deviates from the equilibrium state, and the radiation transmittance and source function need to be calculated on the basis of the specific non-LTE energy level population. Energy level population is a key and difficult problem in the calculation of non-equilibrium radiation. In this paper, the physical process of molecular energy level transition and radiation transfer is studied, including the relationship between molecular transition, radiation spectrum, radiation transfer and energy level distribution. The numerical algorithm for energy level population calculation is established. The non-equilibrium energy level distribution and limb infrared radiation characteristics of CO_2, an important infrared radiation component in the atmosphere, were studied by using the program. The non-equilibrium radiation mechanism of CO_2 4.3μm band under different day and night conditions was analyzed. Finally, the model calculation of CO_2 4.3μm band under different conditions is compared with the limb observation results, and the reliability of the radiation model, calculation method and program are verified.

Keywords: Infrared Radiation; Non-local Thermodynamic Equilibrium (non-LTE); Energy Level Population; CO_2 Radiation.

1. Introduction

The infrared radiation effects of hypersonic aircraft in the near-space region are crucial factors in early warning and penetration design [1, 2]. The detectability of these aircraft is closely related to atmospheric radiation transmission properties such as radiative transmittance and the atmospheric self-radiance. As the altitude increases, the frequency of molecular collisions in the atmosphere decreases, leading to the internal energy, such as vibrational energy level populations, gradually deviating from equilibrium. Near an altitude of 100 km, the predictions of the internationally recognized atmospheric radiation transmission calculation software MODTRAN, which is based on the assumption of equilibrium, differ from measured results by several orders of magnitude [4]. This indicates that non-equilibrium effects must be considered, with the key being the calculation of the non-equilibrium distribution of molecular energy levels. The energy levels of molecules change through interactions with photons or other molecules. Consequently, the distribution of molecular energy levels is influenced by the radiation field of the relevant spectral bands and molecular collision-induced transitions, while the radiation field in turn depends on the local energy level populations and radiation from other atmospheric layers. This interdependence results in considerable complexity. The challenge lies in integrating over frequency, spatial angle, and altitude to couple the solution of the radiative transfer equations with the energy level population equations.

Energy level transitions give rise to spectral bands, and the absorption within these bands leads to energy level transitions. When calculating the contribution of band absorption to energy level transitions, it is necessary to perform a frequency integration within the band to compute the average radiance. Common frequency integration methods can be classified into two categories: line-by-line integration and band models. In the line-by-line integration approach, the spectral lines are divided into multiple intervals based on their shapes, with relatively small changes in the absorption coefficient within each interval. The radiance for all intervals is then summed individually. In the band model approach, the distribution of spectral line intensities within the spectral interval is represented by a simplified model, and simple formulas are used to calculate the average transmittance within the spectral interval. The line-by-line integration method offers high precision but requires significant computational effort. The advantage of the band model is its high computational efficiency, making it suitable for situations where precision requirements are not stringent.

In solving the coupled radiation transfer and statistical equilibrium equations, there are generally two methods: the matrix inversion method and the iterative method. In the matrix inversion method, the radiation transfer equations and the statistical equilibrium equations are solved simultaneously, resulting in a system of equations with a number equal to the product of the number of atmospheric layers (D) and the number of energy levels (L). This necessitates inverting a (D×L)×(D×L) dimensional matrix. When the number of energy levels is large and the atmospheric discretization is significant, the matrix inversion method requires substantial computer memory and is less computationally efficient. However, due to the consideration of both local and non-local effects, the matrix inversion method converges quickly. A typical matrix inversion method is the Curtis matrix method [5, 6], which transforms the radiation transfer equations into equations for the transfer of radiative fluxes. This method has been widely applied in calculating radiative heating (cooling) rates, atmospheric energy budgets, and atmospheric modeling. In the iterative method, the radiation transfer equations and the statistical equilibrium equations are solved iteratively.

After solving the radiation transfer equations to obtain the radiance for all transition bands over D atmospheric layers, the statistical equilibrium equations for L energy levels in each layer are solved, which involves inverting D L×L dimensional matrices. The computational load of the iterative method is smaller, but convergence is slower in optically thick conditions, leading to the development of accelerated iterative methods (ALI). ALI is commonly used to solve multi-level non-equilibrium radiative spectroscopy problems in stellar atmospheres [7]. Software commonly used abroad for non-equilibrium radiation calculations includes the SHARC software [8] and the RFM program [9]. The SHARC software was developed by the United States Air Force Physics Laboratory in the 1990s and can calculate the vibrational level distributions of various atmospheric molecules under different modes, applicable to the altitude range of 30-300 km. SHARC uses older collision mechanisms and spectral data, operates in band mode, with a spectral resolution of 1 cm^{-1}, and has lower computational accuracy; also, the code is not open-source. The RFM model is a line-by-line radiative transfer calculation model [9]. Users input the vibrational temperatures of the energy levels, and through the RFM program, calculations yield optical thickness, atmospheric transmittance, absorption rates, and radiance. The non-equilibrium level distribution is an input parameter for the RFM model; therefore, RFM cannot solve the core problem of energy level distribution in non-equilibrium radiation calculations.

Domestic research on atmospheric radiation primarily focuses on equilibrium radiation studies [10-13], and there is still a significant gap between the research on non-equilibrium radiation and that conducted abroad. In the public literature, there are only studies on the use of the foreign non-equilibrium calculation software SHARC [14, 15], and radiative transfer calculations using the RFM program based on energy level distribution data under specific conditions [16].

The deficiency in the field of non-equilibrium radiation calculation in China has imposed certain limitations on the early warning and penetration design of hypersonic vehicles, as well as on the utilization of atmospheric remote sensing data. In view of this, this paper starts from the fundamental physical processes of non-equilibrium radiation and investigates the relationships between molecular transitions, radiative spectroscopy, radiative transfer, and energy level distribution. The line-by-line method is employed for spectral integration, and the ALI iterative method is used to solve the radiative transfer and statistical equilibrium equations, developing a set of computational programs that can be used to calculate the non-equilibrium state energy level distribution. Finally, the program is applied to study the radiative issues of the important infrared radiative component CO_2 in the atmosphere, analyzing the non-equilibrium radiative mechanism of CO_2, and comparing the results with the publicly available SPIRE and MIPAS detection data from abroad.

2. Physical Model

2.1. Vibrational Energy Level Jumps and Spectral Lines

The frequency of molecular radiation is related to the energy difference between the energy levels before and after the transition. The energy difference for electronic state transitions reaches several electron volts (eV), corresponding to the visible or ultraviolet wavelength range. Vibrational transitions correspond to the spectral region greater than 600 cm^{-1}. The wavenumber for rotational transitions is of the order of 1 cm^-1, corresponding to the far-infrared or microwave bands. Since vibrational transitions are often accompanied by rotational energy level transitions, the molecular vibrational-rotational energy level transition process should be given special attention in the infrared region.

The distribution of the photon energy absorbed by molecules constitutes the spectral lines. Thermal motion of molecules and molecular collision effects will cause Doppler broadening and pressure broadening, respectively. The resulting line shape is known as the Voigt profile, and its expression is given by:

$$k_v = \frac{S}{\alpha_D\sqrt{\pi}}\frac{y}{\pi}\int_{-\infty}^{\infty}\frac{e^{-t^2}\,\mathrm{d}t}{y^2+(x-t)^2} \tag{1}$$

In the formula, v_0 is the central frequency of the spectral line, k_v is the absorption coefficient at frequency v, S is the line strength, and the relationship between the line strength and the absorption coefficient is given by $S=\int_0^{\infty}k_v\mathrm{d}v$. $x=(v-v_0)/\alpha_D$, $y=\alpha_L/\alpha_D$. α_D is the width due to Doppler broadening, and α_L is the width due to pressure broadening. Under standard temperature and pressure (STP) condition, molecular collisions are frequent, and α_L is of the order of 0.1 cm^{-1}, which is one to two orders of magnitude larger than α_D. In this case, the Voigt profile degenerates into a Lorentzian line shape. Above 60 km in high-altitude regions, collisional broadening can be neglected, and the Voigt profile degenerates into a Doppler line shape. For certain non-equilibrium radiation problems, the altitude range may encompass regions where pressure broadening dominates as well as regions where Doppler broadening dominates, hence the adoption of the more complex but universally applicable Voigt line shape. When the atmospheric model is known, it is only necessary to calculate the line shapes at all altitudes at the initial moment.

In the numerical calculations, the energies as well as the spectral parameters of the vibrational transitions of specific molecules can be obtained by querying the database.

2.2. Radiative Transfer Theory

For the infrared band, the radiative scattering effect can be neglected. The interaction between radiation photons and gas molecules can be divided into three processes: (1) molecules spontaneously transition from a higher energy level to a lower one and emit a photon, which is known as spontaneous radiation; (2) under the induction of an incident photon, molecules transition from a higher energy level to a lower one and emit a photon identical to the incident photon, which is referred to as induced radiation; (3) a molecule absorbs a photon and transitions from a lower energy level to a higher one, which is known as radiative absorption.

The radiance, $L_v(P,\vec{s})$, is defined as the radiation energy passing through a unit cross-sectional area per unit solid angle, per unit frequency range, and per unit time at position P in the direction of $\vec{s}$. The rate of change of radiance is directly proportional to the net emission rate (emission minus

absorption) of photons.

Taking the two-energy level problem as an example, the rate of change of radiance along the path according to the spontaneous radiation, induced radiation, and radiation absorption processes can be written as [17]:

$$\frac{dL_v}{ds}\frac{1}{hv}=\frac{n_2A_{21}q_{r,s}}{4\pi}+\frac{n_2B_{21}q_{r,i}L_v}{4\pi}-\frac{n_1B_{12}q_{r,a}L_v}{4\pi} \tag{2}$$

where h is Planck's constant, v is the radiation frequency, L_v is the radiation brightness, and s is the distance along the radiation direction. , n_2 and n_1 are the population distribution of the high and low energy levels of the jump, respectively. Einstein's constants A_{21}, B_{21} and B_{12} are the rate at which a molecule leaps from energy level 2 to energy level 1 by spontaneous radiation, energy level 2 is induced to leap to energy level 1 by photons, and energy level 1 absorbs radiation to leap to 2. Einstein's constant satisfies the relationship: $A_{21}/B_{21}=2hv_0^3/c^2$ and $B_{12}/B_{21}=g_2/g_1.$, c is the speed of light, and , g_1, g_2 are the degree of simplicity of energy levels 1 and 2. , $q_{r,s}$, $q_{r,i}$ and $q_{r,a}$ are the normalized line shapes with respect to spontaneous radiation, excited radiation, and absorption spectral lines.

In the case of spontaneous radiation, for example, $\int_{\Delta v}q_{r,s}\mathrm{d}v=1$ (Δv is the spectral interval of the leap). In general, the absorption and emission spectra of the same leap can be considered to have the same linear shape, i.e. $q_{r,s}=q_{r,a}=q_{r,i}$. Further, Eq. (2) can be organized into the following simplified form

$$\frac{\mathrm{d}L_v}{\mathrm{d}s}=-k_vn_a\left(L_v-J_v\right) \tag{3}$$

where n_a is the number density of radiating molecules and J_v is the radiation source function. Comparison with Eq. (1) and the use of , $\Delta v\ll v$, yields:

$$k_v=\frac{hv}{4\pi n_a}q_{r,a}\left(n_1B_{12}-n_2B_{21}\right) \tag{4}$$

$$J_v=\frac{n_2A_{21}}{n_1B_{12}-n_2B_{21}} \tag{5}$$

At this point, the expressions for the absorption coefficient and the radiation source function, which are the two central physical quantities of the radiative transfer problem, are obtained. From the above equation, it can be seen that the absorption coefficient and radiation source function are related to the energy level spread. Under the thermodynamic equilibrium conditions, the energy level spread satisfies the Boltzmann distribution, and the radiation source function is equal to the Planck function.

2.3. Statistical Equilibrium Theory of Energy Levels

The population of energy levels is primarily determined by radiative and collisional processes. For the vast majority of cases, the rates of radiative transitions and molecular collision rates are much greater than the rates of change of the radiation field and the macroscopic state of the gas. Therefore, it can be considered that the production and loss of molecules at energy levels are in equilibrium, resulting in a constant population of energy levels.

The previous section introduced the relationship between radiation and energy level transitions. This subsection will consider the impact of collisions on energy level transitions. Collisional processes are divided into thermal collisions and non-thermal collisions. In thermal collisions, the higher energy state of the transition is excited by gaining energy from the kinetic energy of the colliding molecules, or the vibrational energy is converted into the kinetic energy of the colliding molecules to de-excite. In non-thermal collisions, such as vibrational-vibrational collisions, electron-vibrational collisions, and chemical reactions, most or even all of the vibrational energy comes from (or goes to) the internal energy of the collision partner.

The thermal collision (V-T) process can be written in the following general form:

$$k_t:\mathrm{n}(2)+\mathrm{M}\rightleftharpoons\mathrm{n}(1)+\mathrm{M}+\Delta E, \tag{6}$$

where k_t is the rate coefficient for the forward process (in $\mathrm{cm^3\ mol^{-1}\ s^{-1}}$), M represents any air molecule, and $\Delta E=E_2-E_1=hv_0$ is the energy difference between the high and low energy levels. The loss rate coefficient of $\mathrm{n}(2)$ is proportional to l_t and k_t , the number density of colliding $[\mathrm{M}]$,i.e. $l_t=k_t[\mathrm{M}]$. For the inverse process n_2 the rate of generation is $k_t'[\mathrm{M}]n_1$, where k_t' is the rate coefficient of the reverse process of Eq.(6), k_t and k_t' satisfies $k'/k_t=g_2/g_1\exp(-hv_0/kT)$. Similarly, the generation rate coefficients of $\mathrm{n}(2)$ can be obtained, which is $p_t=k_t'[\mathrm{M}]$.

For non-thermal collision processes, the vibration-vibration collision process (V-V), for example, is

$$k_{vv}:\mathrm{M}(v)+n(1)\rightleftharpoons n(2)+\mathrm{M}(v')+\Delta E_v \tag{7}$$

Where $\mathrm{M}(v)$ is the atmospheric molecule in the vibrational excited state v, in the excited state v' after the collision, and the energy before and after the collision $E_v>E_{v'}$, $\Delta E_v=E_v-E_{v'}-hv_0$. k_{vv} is the rate coefficient for the forward process, and that for the reverse process is k_{vv}' , both of which satisfy the relation $k_{vv}'/k_{vv}=g_1g_v/g_2g_{v'}\exp(-\Delta E_v/kT)$. In the following, the generation and loss rate coefficients for the non-thermal collision process are denoted by p_{nt} and l_{nt}, respectively.

For the two-energy-level problem, under statistical equilibrium conditions, the net production n_2 by radiative processes and the net loss n_2 by collisional processes cancel each other out.

$$n_2A_{21}+n_2B_{21}\overline{L}_{\Delta v}-n_1B_{12}\overline{L}_{\Delta v}+\left(l_t+l_{nt}\right)n_2-\left(p_t+p_{nt}\right)n_1=0 \tag{8}$$

Eq.(8) is the statistical equilibrium equation for the two energy levels, where $\overline{L}_{\Delta v}$ is the average radiance in the spectral band interval and spatial direction, i.e.

$$\bar{L}_{\Delta v}=\frac{1}{4\pi}\int_{\omega}\int_{\Delta v}L_v q_{r,a}(v)\,dv d\omega \tag{9}$$

Similarly, for the multi-energy level problem, the statistical equilibrium equation for the energy level m can be written as

$$\sum_{j<m}\frac{A_{mj}n_m-\left(B_{jm}n_j-B_{mj}n_m\right)\bar{L}_{mj}}{hv_{mj}}-\sum_{j>m}\frac{A_{jm}n_j-\left(B_{mj}n_m-B_{jm}n_j\right)\bar{L}_{jm}}{hv_{jm}}+\sum_{j\neq m}\left(n_m C_{mj}-n_j C_{jm}\right)=0 \tag{10}$$

where $\bar{L}_{mj}$ is the average radiance of the band of the jump from the energy level m to the energy level j, and is the rate coefficient for the conversion of the energy level to the energy level by collision. In the two-energy-level problem, C_{mj} corresponds to l_t+l_{nt} in Eq.(9). When the number of energy levels to be sought is N, equation (10) is established for N-1 energy levels, and combined with $\sum_{m=1,N}n_m=n_a$, the system of statistical equilibrium equations (SEE) for the energy levels to be sought can be obtained.

3. Numerical Calculation Method

Due to the presence of the mean radiance $\bar{L}_{\Delta v}$ in the system of statistical equilibrium equations , coupling the RTE is required to solve the SEE to obtain L_v. To simplify the calculation, the following assumptions are used [17]:

(1) The rate of change of planetary atmospheres and radiation in the vertical direction is much greater than that in the horizontal direction. Therefore, a parallel plane atmospheric model is adopted, as shown in Figure 1, where it is only necessary to solve for the energy level population varying along one-dimensional vertical direction;

(2) Within the same vibrational energy level, the rotational energy level spacing (1 cm^{-1}) is much smaller than the vibrational energy level spacing (~100 cm^{-1}). Compared to vibrational energy levels, rotational energy levels require significantly fewer collisions to maintain an equilibrium distribution. Hence, adopting the assumption of rotational equilibrium can greatly reduce the computational load;

(3) In non-equilibrium region, the half-width of the spectral lines is of the order of 0.001 cm^{-1}, which is much smaller than the spacing between rotational and vibrational spectral lines. Therefore, it is considered that spectral lines of different transition bands do not overlap. The absorption coefficients for each transition band are calculated independently, as well as the impact of radiative transitions on the energy level population.

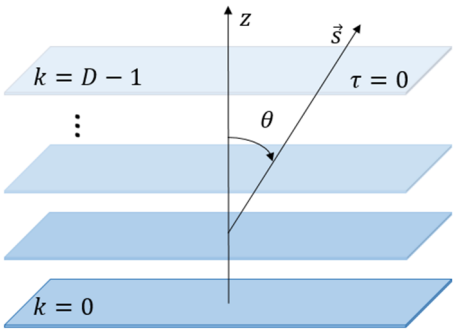

Fig 1. An illustration of plane-parallel approximation

References are cited in the text just by square brackets [1]. (If square brackets are not available, slashes may be used instead, e.g. /2/.) Two or more references at a time may be put in one set of brackets [3, 4]. The references are to be numbered in the order in which they are cited in the text and are to be listed at the end of the contribution under a heading References, see our example below.

Defining optical thickness under the parallel plane atmosphere assumption

$$\tau_{v,\mu}(z)=\frac{1}{\mu}\int_z^{\infty}k_v n_a\,\mathrm{d}z \tag{11}$$

where $\mu=\cos(\theta)$ is the direction angle cosine. Combined with $\tau_{v,\mu}(z)$, the radiative transfer equation i.e. Eq. (3) can be written as

$$\mathrm{d}L_{v,\mu}\left(\tau_{v,\mu}\right)/\mathrm{d}\tau_{v,\mu}=L_{v,\mu}\left(\tau_{v,\mu}\right)-J_{v,\mu}\left(\tau_{v,\mu}\right) \tag{12}$$

The above equation has an analytic

$$L_{v,\mu}(z)=L_{v,\mu}(z_0)\mathrm{e}^{\tau_{v,\mu}(z)-\tau_{v,\mu}(z_0)}+\int_{\tau_{v,\mu}(z_0)}^{\tau_{v,\mu}(z)}J_{v,\mu}\,\mathrm{e}^{\tau_{v,\mu}(z)-\tau_{v,\mu}(z')}\mathrm{d}\tau_{v,\mu}(z') \tag{13}$$

The above equation states that the radiance at a given position and direction is equal to the part of the boundary radiance that reaches that position after absorption, plus the part of all the radiation sources along the path that reaches that position after absorption. For upward radiation, $\mu>0$, z_0 is located at the lower boundary, and for downward radiation, $\mu<0$, z_0 is located at the upper boundary. For simplicity, the subscript "v,μ" is omitted in the following writing without ambiguity.

For the division of the atmosphere into D layers, as shown in Fig. 1, the source function of the integral term in Eq. (13) is discretized numerically, and the source function is approximated by a first-order or higher-order approximation, i.e.

$$J(\tau)=\mathcal{L}\left(...,J^k,J^{k+1},...\right),\tau^{k+1}<\tau<\tau^k \tag{14}$$

where $\mathcal{L}$ denotes a linear function, and substituting into Eq. (13), the general form of the numerical solution for the radiance can be obtained as follows

$$\begin{pmatrix}L^0\\L^1\\\vdots\\L^{D-1}\end{pmatrix}=\begin{pmatrix}\Lambda^{0,0}&\Lambda^{0,1}&\cdots&\Lambda^{0,D-1}\\\Lambda^{1,0}&\Lambda^{1,1}&\cdots&\Lambda^{1,D-1}\\\vdots&\vdots&\cdots&\vdots\\\Lambda^{D-1,0}&\Lambda^{D-1,1}&\cdots&\Lambda^{D-1,D-1}\end{pmatrix}\begin{pmatrix}J^0\\J^1\\\vdots\\J^{D-1}\end{pmatrix}$$

The above equation can be written in the simple form

$$L=\Lambda J \tag{15}$$

Λ is a function of $\tau_{v,\mu}$. In the case of upward radiation, for example, the matrix Λ is an upper triangular matrix when using the first-order approximation. The diagonal elements of the matrix Λ represent the influence of the local source function on the radiance. The method of calculating the radiance using Eq. (13) and (14) is called the short eigen

method, and the second-order short eigen method is used in this paper to improve the accuracy [18].

After finding the radiance in all frequency domains and spatial angles, the spectral bands can be integrated over frequency intervals and spatial angles to obtain the average irradiance for each jump, i.e.

$$\overline{L}_{\Delta v} = \sum_{v}\sum_{\mu} \phi_v \gamma_\mu L_{v,\mu} \tag{16}$$

where " $\overline{\ }$ " denotes the average over the frequency domain and spatial angle of the spectral band, ϕ_v and γ_μ are the weight functions over the frequency domain and spatial angle, respectively. ϕ_v is proportional to the product of the absorption coefficient of the spectral line and the spectral line discrete width. The spatial angle discretization is generally done by Gaussian quadrature method to select the discretization points and weights.

When solving the statistical equilibrium equations in conjunction with the mean radiance, the local source function takes the value of the next step to accelerate the iterative convergence process, which is known as accelerated algorithmic Λ iteration (ALI) [7, 17, 18].

Decompose Λ into the diagonal array Λ^* and $\Lambda - \Lambda^*$, i.e.

$$\overline{L}_{\Delta v} = \overline{\Lambda} J = \overline{\Lambda}^* J + \overline{L}^{eff}_{\Delta v} \tag{17}$$

From the above equation, it can be seen that the contribution of the non-local source function on the transmission path to the mean radiance $\overline{L}^{eff}_{\Delta v} = \left(\overline{\Lambda} - \overline{\Lambda}^*\right) J$. In the $i+1$ iteration, the mean irradiance in the radiative jump band from l to l' ($l > l'$) is written as

$$\overline{L}^{i+1}_{ll'} = \overline{\Lambda}^{*,i}_{ll'} J^{i+1}_{ll'} + \overline{L}^{eff,i}_{ll'} \tag{18}$$

Combined with the Eq. (5) for the source function, the numerical solution format for the energy level statistical equilibrium Eq. (10) can be obtained as

$$\sum_{l'<l}\left[n_l^{i+1}A_{ll'}\left(1-\overline{\Lambda}^{*,i}_{ll'}\right)-\left(n_{l'}^{i+1}B_{l'l}-n_l^{i+1}B_{ll'}\right)\overline{L}^{eff,i}_{ll'}\right]-\sum_{l'>l}\left[n_{l'}^{i+1}A_{l'l}\left(1-\overline{\Lambda}^{*,i}_{ll'}\right)-\left(n_l^{i+1}B_{ll'}-n_{l'}^{i+1}B_{l'l}\right)\overline{L}^{eff,i}_{ll'}\right]+$$
$$\sum_{l'}\left[n_l^{i+1}C_{ll'}-n_{l'}^{i+1}C_{l'l}\right]=0 \tag{19.a}$$

The number of equations included in the above system of equations is the number of energy levels to be solved, replacing the conservation equation for the last energy level by

$$\sum_{l} n_l^{i+1} = n_a \tag{19.b}$$

the system of equations is closed now.

When solving the radiative transfer equation, after obtaining $\overline{\Lambda}^*$ and $\overline{L}^{eff}_{\Delta v}$, we substitute (19.a) and invert the coefficient matrix of the statistical equilibrium equations to obtain the energy level distribution. Fig.2 shows the coupled solution process of the radiative transfer equation and the statistical equilibrium equation.

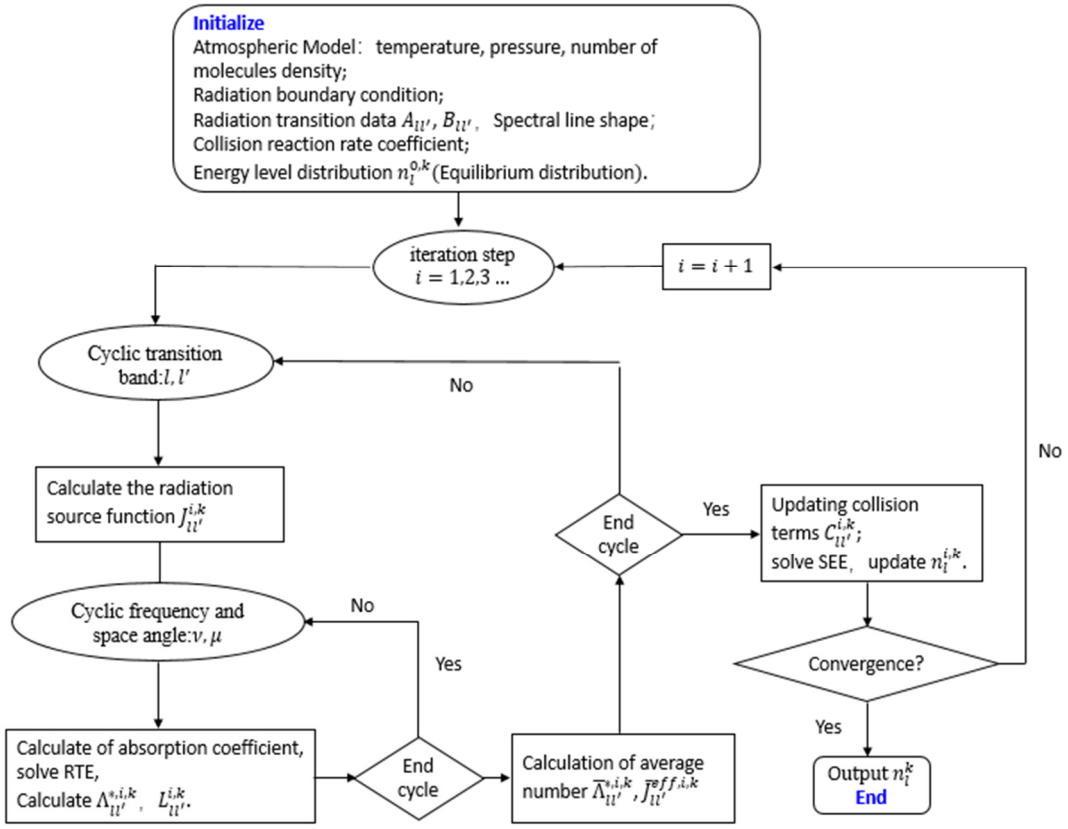

Fig 2. Calculation procedure for populations of non-LTE states. l and l': energy levels. i: iteration step. k: atmospheric layer

4. CO_2 Non-equilibrium Radiative Energy Level Distribution

CO_2 is an important component of the Earth's limb atmospheric infrared radiation. CO_2 participates in the atmospheric thermal cycle through infrared cooling and heating, exerting a significant impact on the thermal structure of the atmosphere; the 15 μm and 4.3 μm bands of CO_2 are crucial for limb atmospheric environmental detection and military target early warning.

CO_2 is a triatomic molecule with three vibrational modes: symmetric stretch (ν_1), symmetric bend (ν_2), and asymmetric stretch (ν_3). The symmetric stretch mode (ν_1) does not change the molecular dipole moment and is inactive in the infrared radiation band; the symmetric bend mode (ν_2) is doubly degenerate, corresponding to the 15 μm band. The asymmetric stretch mode (ν_3) corresponds to the 4.3 μm band. In addition, CO_2 also has many hot bands, combination bands, and isotopic bands.

This paper includes calculations for four CO_2 isotopologues, with a total of 22 energy levels, as detailed in Table 1. The spectral line parameters are obtained from the HITRAN database [19, 20]. This work references the collisional reaction model from literature [9], as shown in Table 2, with reaction rates consistent with those in literature [9]. Processes 1-2 represent thermal collisions between neutral molecules and CO_2, while processes 3-8 involve vibrational energy levels of CO_2 in V-V transitions. The energy of the first vibrational state of N_2 is close to the energy gap of the asymmetric stretch vibrational state of CO_2, leading to near-resonance V-V transfers between the two, as shown in process 6. Therefore, it is necessary to simultaneously solve the statistical equilibrium equations for both N_2 and $N_2(1)$. Processes 9-11 show the main collisional processes affecting $N_2(1)$.

Table 1. CO_2 vibrational energy levels

Number	Isotopes	Energy level	Energy (cm^{-1})	Concurrency
1	626	00001	0.0000	1
2	626	01101	667.3801	2
3	626	10002	1285.4087	1
4	626	02201	1335.1317	2
5	626	10001	1388.1847	1
6	626	11102	1932.4702	2
7	626	03301	2003.2463	2
8	626	11101	2076.8557	2
9	626	00011	2349.1433	1
10	626	01111	3004.0122	2
11	626	10012	3612.8417	1
12	626	02211	3659.2728	2
13	626	10011	3714.7828	1
14	636	00001	0.0000	1
15	636	01101	648.4784	2
16	636	00011	2283.4876	1
17	636	01111	2920.2387	2
18	628	00001	0.0000	1
19	628	01101	662.3734	2
20	628	00011	2332.1128	1
21	627	00001	0.0000	1
22	627	01101	664.7289	2
23	627	00011	2340.0136	1

According to the collisional reaction mechanism, the atmospheric components that affect the energy level distribution of CO_2 include: N_2, O_2, CO_2, O, $O(^1D)$, and $O_2(1)$. The atmospheric model used is consistent with that in literature [9], with specific reference to the supporting documentation.

For ease of analysis and comparison, the energy level distribution is converted into the corresponding vibrational temperatures. The expression for vibrational temperature is given by:

$$T_v = -\frac{E_v}{k_B \ln\left(n_v g_0 / n_0 g_v\right)} \tag{20}$$

Where k_B is Boltzmann constant, n_0, n_v is the ground state, the vibrational state of the population distribution, g_0, g_v is the degree of simplicity of the ground state, vibrational state, E_v is the energy of vibrational state . The higher the vibrational temperature of the energy level, the higher population distribution of energy level populations relative to the equilibrium state.

Fig.3 shows a comparison of the vibrational temperatures of energy levels related to the 15 μm band with the atmospheric thermodynamic temperature under conditions of October, 45° north latitude, and a solar zenith angle of 44.5° during the day, with the black line representing the atmospheric dynamic temperature. Figure 4 shows the vibrational temperatures of energy levels related to the 2.7 μm and 4.3 μm bands under the same conditions.

From Fig.3, it can be observed that for the 12C16O2(v_2) energy levels, below 70 km, thermal collision is the dominant process, and the vibrational temperature of 12C16O2(v_2) is consistent with the atmospheric dynamic temperature, with

the energy level populations satisfying the Boltzmann distribution.

Table 2. Collision processes affecting the CO_2 vibration levels

Number	Crash course
1a	$CO_2^i(\nu_2)+N_2 \rightleftharpoons CO_2^i(\nu_2-1)+N_2$
1b	$CO_2^i(\nu_2)+O_2 \rightleftharpoons CO_2^i(\nu_2-1)+O_2$
1c	$CO_2^i(\nu_2)+O \rightleftharpoons CO_2^i(\nu_2-1)+O$
2a	$CO_2^i(\nu_2,\nu_3)+N_2 \rightleftharpoons CO_2^i(\nu_2+2,3 \text{ or } 4,\nu_3-1)+N_2$
2b	$CO_2^i(\nu_2,\nu_3)+O_2 \rightleftharpoons CO_2^i(\nu_2+2,3 \text{ or } 4,\nu_3-1)+O_2$
2c	$CO_2^i(\nu_2,\nu_3)+O \rightleftharpoons CO_2^i(\nu_2+2,3 \text{ or } 4,\nu_3-1)+O$
3	$CO_2^i(\nu_2,\nu_3)+CO_2^j \rightleftharpoons CO_2^i(\nu_2+1,\nu_3-1)+CO_2^j(\nu_2=1)$
4	$CO_2^i(\nu_2,\nu_3)+O_2 \rightleftharpoons CO_2^i(\nu_2+1,\nu_3-1)+O_2(1)$
5a	$CO_2^i(\nu_2)+CO_2^j \rightleftharpoons CO_2^i(\nu_2-1)+CO_2^j(\nu_2=1)$
5b	$CO_2^i(\nu_2)+CO_2^j(\nu_2') \rightleftharpoons CO_2^i(\nu_2-1)+CO_2^j(\nu_2'+1)$
6	$CO_2^i(\nu_2,\nu_3)+N_2 \rightleftharpoons CO_2^i(\nu_2,\nu_3-1)+N_2(1)$
7	$CO_2^i(\nu_1,\nu_2,\nu_3)+N_2 \rightleftharpoons CO_2^i(\nu_1',\nu_2',\nu_3)+N_2$
8	$CO_2^i(\nu_3)+CO_2^j(\nu_3') \rightleftharpoons CO_2^i(\nu_3-1)+CO_2^j(\nu_3'+1)$
9	$N_2+O(^1D) \rightarrow N_2(1)+O$
10	$N_2(1)+O_2 \rightleftarrows N_2+O_2$
11	$N_2(1)+O \rightleftarrows N_2+O$

Note: The superscripts i, j in the table indicates the isotope numbers.

During the day, the absorption of 2.7 μm solar radiation excites the 10012, 02211, and 10011 levels, and the absorption of 4.3 μm solar radiation directly excites the 00011 energy level, causing the vibrational temperature of the () energy levels to deviate from equilibrium starting at an altitude of 50 km and to be higher than the dynamic temperature. Between 70-105 km, as the thermal collision process weakens, and the relaxation due to ν_3 quantum emission or collisions (processes 2-4, 6) occurs, the vibrational temperature of the ν_2 energy level is greater than the dynamic temperature; similarly, related to the ν_3 relaxation processes of the quantum, the higher the energy level, the higher the vibrational temperature. Above the lower thermosphere, the atmosphere absorbs ultraviolet radiation, causing a sharp rise in temperature, and the thermal collision process weakens with increasing altitude, resulting in vibrational temperatures lower than the dynamic temperature. Above the lower thermosphere, the energy levels related to the 2.7 μm and 4.3 μm bands are mainly influenced by solar radiation absorption and emission, with the vibrational temperatures trending towards stability with altitude; for the vibrational energy levels related to the 15 μm band, the energy level distribution is primarily influenced by the absorption of the lower atmospheric radiative flux and radiative emission, with the vibrational temperature decreasing with increasing altitude.

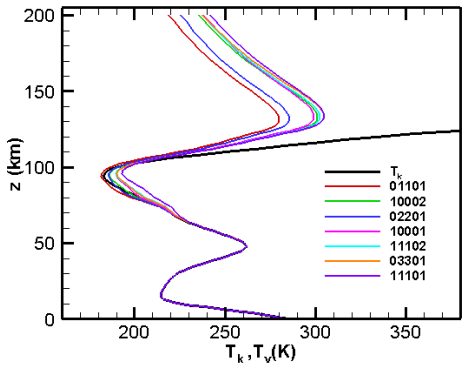

Fig 3. Vibrational temperatures for the $^{12}C^{16}O_2(\nu_2)$ levels at daytime.

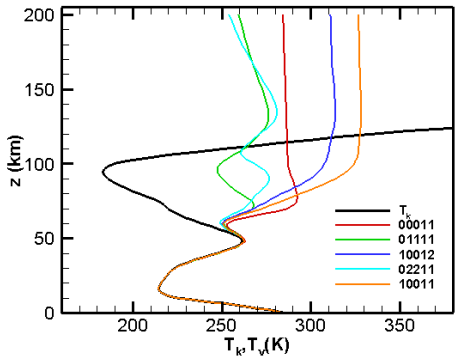

Fig 4. Vibrational temperatures for the $^{12}C^{16}O_2(\ ^{v_3}\ )$levels at daytime

Figure 5 shows a comparison of the vibrational temperatures of energy levels related to the 15 μm band with the atmospheric thermodynamic temperature under conditions of October, 45° latitude north, during the night. Figure 6 shows the vibrational temperatures of energy levels related to the 2.7 μm and 4.3 μm bands under the same conditions.

From Figure 5, it can be observed that below 80 km, the vibrational temperatures of the 12C16O2 (v_2) energy levels are consistent with the atmospheric dynamic temperature. Above 80 km, there is a deviation from equilibrium. At the same altitude, energy levels with higher energy, such as the 11101 level, have higher vibrational temperatures, while energy levels with lower energy, such as the 01101 level, have lower vibrational temperatures, which is related to the strength of the spectral bands. This is because the 11101 level produces a weaker 15 μm second thermal band, and compared to the fundamental band, the lower atmosphere is optically thinner, allowing for the absorption of more radiation from the warmer lower atmosphere. Similarly, energy levels with even higher energy and related bands that are optically thinner can absorb more radiative flux from the lower atmosphere, resulting in vibrational temperatures that are higher than the local dynamic temperature from about 65 km to approximately 105 km, as shown in Figure 6. It is further evident that the vibrational temperature distributions of energy levels with similar energies, such as 10012, 02211, and 10011, differ very little. Due to the effect of radiative cooling, the vibrational temperatures of all energy levels are below the dynamic temperature above 100-105 km.

In summary, solar radiation, the cold space environment, the vertical temperature structure, and atmospheric thinning are the main factors causing CO_2 to deviate from equilibrium distribution. Energy level v_3 with higher energy deviate from equilibrium at lower altitudes than energy level v_2 with lower energy. During the day, at middle atmospheric heights, energy level v_3 absorb solar radiation, causing the vibrational temperature to be higher than the dynamic temperature, and subsequently, through collisional and radiative relaxation, the energy level v_2 begin to exceed the dynamic temperature at an altitude of 70 km. At night, the middle atmospheric energy level v_3 absorb radiative flux from the warm stratospheric layer, causing them to exceed the dynamic temperature starting at an altitude of 65 km. Around the lower thermosphere at altitudes of 100-105 km, the primary atmospheric components experience a sharp rise in temperature due to the absorption of ultraviolet radiation. Owing to the thinning atmosphere and lower collision frequencies, as well as the radiative cooling to the space environment, the vibrational temperatures exhibit a non-equilibrium state below the dynamic temperature.

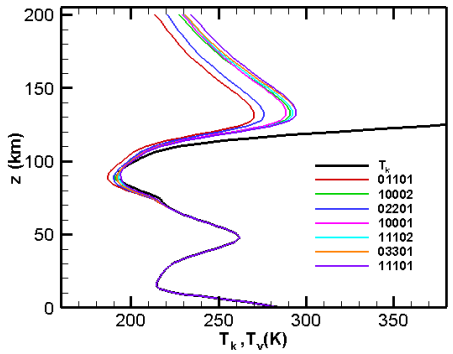

Fig 5. Vibrational temperatures for the $^{12}C^{16}O_2(\ ^{v_2}\ )$levels at night-time

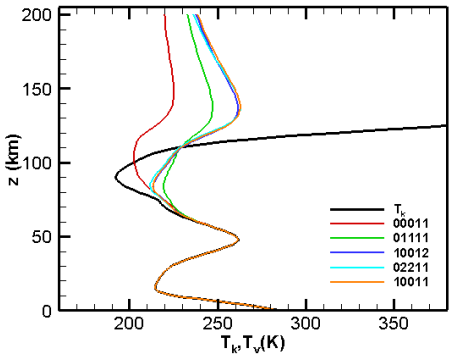

Fig 6. Vibrational temperatures for the $^{12}C^{16}O_2(\ ^{v_3}\ )$levels at night-time

5. Comparison of Numerical and Experimental Calculations of Limb Radiance

Limb detection sensing, due to its unique advantage of traversing only through the atmosphere, is particularly suited for high-altitude atmospheric detection. Representative examples include the 1977 SPIRE sounding rocket experiment [21]; the MIPAS instrument launched by the European Space Agency (ESA) in March 2002, which was carried on the EVISAT satellite [22]; and the SABER instrument launched by NASA in 2002, which was carried on the TIMED satellite [23]. Combined with numerical simulations, infrared sensing data plays a crucial role in atmospheric remote sensing and modeling [24-30]. This section will compare the calculated results of the 4.3 μm edge-of-atmosphere radiance of CO_2 with experimental results to validate the correctness of the non-equilibrium radiative calculation model presented in this paper.

5.1. Comparison with SPIRE Data

The SPIRE experiment was a rocket test conducted by the United States on September 28, 1977, in Alaska. It operated in the wavelength range of 1.4-16.5 μm and obtained infrared spectral bands such as the CO_2 4.3 μm band under daytime and nighttime conditions. The experiment measured the

background radiation brightness distribution of the limb atmosphere with respect to tangential altitude.

To simulate the experimental conditions, an atmospheric model and illumination conditions were adopted for early October at 45°N, 10 am and 10 pm, respectively. Based on the calculated changes in energy level distribution with altitude (see Section 3), the RFM package was used to calculate the changes in limb radiance with tangential altitude.

Fig.7 compares the measured and calculated limb radiance of the CO_2 4.3 μm band during the daytime. The SPIRE experiment conducted multiple scans of the daytime side atmosphere, and the data from different scans showed very small deviations. Figure 7 shows the results of the 9th scan. To compare with the equilibrium state, the calculated results of equilibrium state radiation under the same conditions are also shown. It can be seen from the figure that the non-equilibrium state calculation results are in good agreement with the experimental detection results up to 140 km, well reproducing the variation law of limb radiance with altitude. At about 42 km altitude, a "knee point" appears in the radiance profile, below which the radiance changes little with altitude, and above which the radiance decreases rapidly with altitude. At about 68 km altitude, a second knee point appears in the non-equilibrium calculation, which was not observed in the experimental results, possibly due to the experiment being conducted in a more northern location. Below 50 km, there is almost no deviation between the experimental and non-equilibrium calculation results, and the deviation between the calculation results and the experimental measurements is less than 50% between 50-140 km. Compared with the equilibrium state calculation results, it can be seen that the daytime 4.3 μm radiation deviates from the equilibrium state starting at about 50 km, consistent with the calculated results of the energy level distribution.

Fig.8 compares the measured and calculated limb radiance of the CO_2 4.3 μm band under nighttime conditions. The nighttime radiance is one order of magnitude lower than the daytime at 100 km altitude. Due to the large errors in the nighttime measurement results above 100 km altitude, only the data below 100 km is shown in the figure. The radiation measurement and non-equilibrium calculation results are in good agreement below 56 km, and the relative deviation is about 50% between 56-100 km.

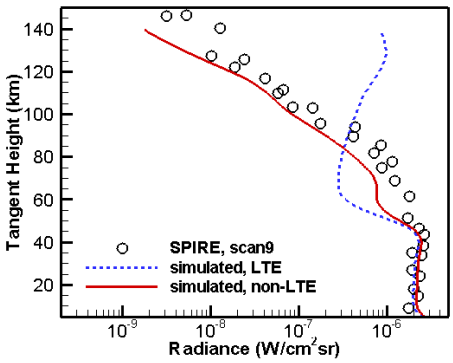

Fig 7. CO_2 4.3μm band limb radiance at daytime, comparison of data measured by SPIRE and calculated by LTE and non-LTE model, with autumn-daytime atmosphere at mid-latitude of north semi-sphere

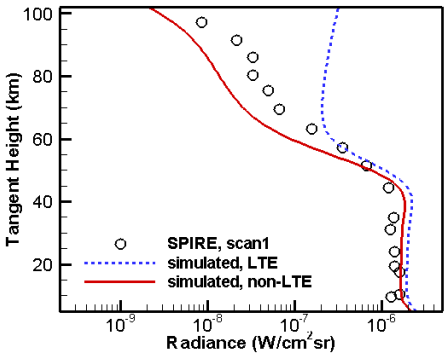

Fig 8. As Fig. 7, but at night

5.2. Comparison with MIPAS Data

The MIPAS instrument has a spectral range of 4.15-14.6 μm, divided into five sub-bands, with a spectral resolution of 0.0625 cm^{-1}. This section compares the calculated results of the CO_2 4.3 μm band with the spectral measurements of the MIPAS in the range of 2200-2400 cm^{-1}.

The experimental detection conditions were set for midday on July 15, 2009, during the daytime. The atmospheric model and solar illumination conditions for mid-July in the Northern Hemisphere at middle latitudes, at 10 am, were adopted in the calculations [9]. The energy level distribution with altitude was calculated using an unbalanced model. On this basis, the RFM package was used to calculate the radiation spectrum and radiance along the limb path.

Fig.9 compares the MIPAS measured results, the equilibrium state, and the non-equilibrium state calculated results of the CO2 4.3 μm limb radiance. It can be seen from the figure that the equilibrium state and non-equilibrium state calculated results exhibit the first "knee point" at about 40 km, and the first "knee point" of the detection data is slightly higher, at about 41 km. Above 40 km, the radiation begins to deviate from the equilibrium state. The non-equilibrium calculation results reach a minimum at 60 km altitude, and between 60-70 km, the radiance increases with the tangential altitude, and above 70 km, it decreases with increasing altitude. The detection data is slightly larger than the calculated results above 50 km altitude, with a local minimum in radiance at 65 km altitude and a local maximum at 71 km altitude.

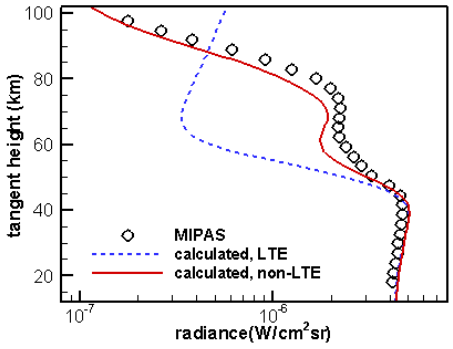

Fig 9. CO_2 4.3 μm band limb radiance at daytime, at summer of mid-latitude of north semi-sphere.

Overall, the non-equilibrium calculation model in this paper can replicate the law of atmospheric background radiation changing with altitude under different seasons and day-night conditions. Below 50 km altitude, the non-equilibrium calculation results are in good agreement with the experimental measurements, and above 50 km, the non-

equilibrium calculation results have a deviation of less than 50% compared to the experimental measurements. The deviation between the experimental and calculated results is mainly related to the experimental measurement error, the atmospheric temperature and pressure model, the atmospheric composition model, and the collision model and rate [27, 31-33]. The uncertainty of some trace components and collision rate coefficients is the main reason for the uncertainty in non-equilibrium calculations. To further improve the calculation accuracy of the model, it is necessary to conduct research in conjunction with atmospheric models and collision models.

Fig.10 shows the contours of the ratio of the calculated equilibrium to non-equilibrium IR irradiance versus altitude under diurnal and nocturnal conditions. It can be seen from the figure that under night conditions, the radiance calculated by non-LTE model is smaller than that calculated by LTE mdel for altitudes higher than 45km. At daytime, the non-LTE radiance is larger than LTE radiance for altitdues between 45km and 90km.

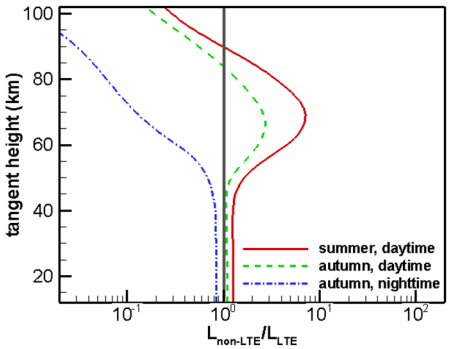

Fig 10. The ratio of limb radiance calculated by non-LTE model to that calculated by LTE model for CO_2 4.3 μm band in different conditions.

6. Summary

This paper investigates the computational methods for atmospheric infrared non-equilibrium radiation. By utilizing the short characteristic method to solve the radiation transfer equations and adopting the ALI (Accelerated Lambda Iteration) method for iterative solution of the statistical equilibrium equations, a computational algorithm for solving the non-equilibrium energy level populations is constructed. An atmospheric non-equilibrium radiation transmission and energy level distribution calculation program is independently developed. The non-equilibrium state energy level distribution and limb infrared radiation characteristics of important infrared radiation components in the atmosphere, such as CO_2, are studied. The non-equilibrium radiation mechanisms of the CO_2 15 μm and 4.3 μm bands are analyzed.

Above the thermosphere, the non-equilibrium effects of radiation are primarily due to radiation cooling and atmospheric thinning. For middle atmospheric heights, during the daytime, the non-equilibrium effects of the 4.3 μm band are mainly caused by the absorption of solar radiation, while the non-equilibrium effects of the long-wave 15 μm band are primarily due to the collisions and radiative relaxation of the energy level. During the nighttime, the non-equilibrium effects of the 4.3 μm band are mainly derived from the absorption of radiative flux from the warmer lower atmosphere. The 4.3 μm band deviates from equilibrium above approximately 50 km during the day and above approximately 60 km at night. The 15 μm band deviates from equilibrium above 70 km during the day and above 80 km at night.

The calculated results of limb radiance are compared with the limb detection results of SPIRE and MIPAS. The calculated results are in good agreement with the experimental data, with a relative deviation of less than 50%.

This work addresses deficiencies in the calculation of atmospheric non-equilibrium radiation energy level distribution in China and is of significant importance for modeling the non-equilibrium radiation mechanisms in the atmosphere, as well as for domestic aircraft infrared detection and atmospheric modeling research.

References

[1] Fan J, Cong BB, Wang J, Chen H, Wan T, Li SH, Analysis of signal-to-noise ratio for space-based infrared detection of intercontinental glide vehicles. SCIENTIA SINICA Physica, Mechanica & Astronomica, 2020, 50(5): 122-130. (in Chinese)

[2] Li S, Wang Y, Fan J, Study on the Influence of Atmospheric Environment on Space Infrared Detection, Abstracts of the 12th Chinese Conference on Physics and Mechanics, 2012, p97

[3] Available from: http://modtran.spectral.com/.

[4] Wang J, Numerical Simulation of Atmospheric Limb Infrared Radiation and Nonequilibrium Effects, 2022, University of Chinese Academy of Sciences.

[5] Funke B, López-Puertas M, García-Comas M, et al., GRANADA: A Generic RAdiative traNsfer AnD non-LTE population algorithm. Journal of Quantitative Spectroscopy and Radiative Transfer, 2012, 113(14): 1771-1817.

[6] Curtis AR, Goody RM, Thermal Radiation in the Upper Atmosphere. Proceedings of the Royal Society of London Series A-Mathematical and Physical Sciences, 1956, 236 (1205): 193-206.

[7] Kutepov AA, Gusev OA, Ogibalov VP, Solution of the non-LTE problem for molecular gas in planetary atmospheres: superiority of accelerated lambda iteration. Journal of Quantitative Spectroscopy & Radiative Transfer, 1998, 60(2): 199-220.

[8] Gruninger JH, Sundberg RL, Acharya PK, et al., User's Manual For SHARC-4 The Strategic High-Altitude Radiance Code. . 1997, PHILLIPS LAB HANSCOM AFB MA.

[9] Dudhia A, The Reference Forward Model (RFM). Journal of Quantitative Spectroscopy and Radiative Transfer, 2017, 186: 243-253.

[10] Shi Guangyu, Atmospheric Radiology. 2007, Beijing: Science Book Press.

[11] Zhang H, Shi G, A Fast and Efficient Line-By-Line Calculation Method for Atmospheric Adsorption. Chinese Journal of Atmospheric Sciences, 2000, 1: 111-121. (in Chinese)

[12] Wei H, Chen X, Dai C, Combined Atmospheric Radiative Transfer (CART) Model and Its Applications. Infrared and Laser Engineering, 2012, 41(12): 3360-3366. (in Chinese)

[13] Guo J, Research On Spectral Radiation Properties of Limb Atmospheric Background, 2015, University of Electronic Science and Technology of China.

[14] Dai C, The application Research 0n the In[rared Atmospheric Radiative Model for Middle and Upper Atmosphere, 2013, The Chinese Academy of Science.

[15] Liu D, Dai C, Wei H, Comparison of LTE and non—LTE for Limb Infrared Radiation SimuIation of Middle and Upper Atmosphere. Journal of Atmospheric and Environmental Optics, 2019, 14: 337-344. (in Chinese)

[16] Tan P, Non-LTE Limb IR Radiances Calculation in the Upper Atmosphere, 2015, Nanjing University of Science & Technology.

[17] López-Puertas M, Taylor FW, Non-LTE Radiative Transfer in the Atmosphere. 2001, Singapore: World Scientific.

[18] Hubený I, Mihalas D, Theory of Stellar Atmospheres An Introduction to Astrophysical Non-equilibrium Quantitative Spectroscopic Analysis. 2015, New Jersey: Princeton University Press.

[19] Available from: https://hitran.org/.

[20] Gordon IE, Rothman LS, Hargreaves RJ, et al., The HITRAN2020 molecular spectroscopic database. Journal of Quantitative Spectroscopy and Radiative Transfer, 2022, 277: 107949.

[21] Stair AT, Sharma RD, Nadile RM, et al., Observations of limb radiance with Cryogenic Spectral Infrared Rocket Experiment. Journal of Geophysical Research: Space Physics, 1985, 90(A10): 9763-9775.

[22] Fischer H, Birk M, Blom C, et al., MIPAS: an instrument for atmospheric and climate research. Atmospheric Chemistry and Physics, 2008, 8: 2151-2188.

[23] Available from: https://saber.gats-inc.com/.

[24] López-Puertas M, Funke B, Jurado-Navarro ÁA, et al., Validation of the MIPAS CO2 volume mixing ratio in the mesosphere and lower thermosphere and comparison with WACCM simulations. Journal of Geophysical Research: Atmospheres, 2017, 122(15): 8345-8366.

[25] Kiefer M, von Clarmann T, Funke B, et al., IMK/IAA MIPAS temperature retrieval version 8: nominal measurements. Atmospheric Measurement Techniques, 2021, 14(6): 4111-4138.

[26] Esplin R, Mlynczak MG, Russell J, et al., Sounding of the Atmosphere Using Broadband Emission Radiometry (SABER): Instrument and Science Measurement Description. Earth and Space Science, 2023, 10(9).

[27] Das S, Bailey SM, Hervig ME, et al., Validation of Version 1.3 Ozone Measured by the SOFIE Instrument. Earth and Space Science, 2023, 10(10).

[28] Emmert JT, Jones M, Siskind DE, et al., NRLMSIS 2.1: An Empirical Model of Nitric Oxide Incorporated Into MSIS. Journal of Geophysical Research: Space Physics, 2022, 127(10).

[29] Zeng D, Wan T, Li S, Study of the Temporal-Spatial Fluctuations and Empirical Model of Near Space Atmospheric Density, Chinese Journal of Theoretical and Applied Mechanics, 2022, 54(11): 2984-2993. (in Chinese)

[30] Garcia RR, On the Structure and Variability of the Migrating Diurnal Temperature Tide Observed by SABER. Journal of the Atmospheric Sciences, 2023, 80(3): 687-704.

[31] von Clarmann T, Glatthor N, Grabowski U, et al., TUNER-compliant error estimation for MIPAS: methodology. Atmospheric Measurement Techniques, 2022, 15(23): 6991-7018.

[32] Eckermann SD, Augmented Non-LTE Parameterization of NO Infrared Radiative Cooling Rates. Journal of Geophysical Research-Space Physics, 2023, 128(2).

[33] Raspollini P, Arnone E, Barbara F, et al., Level 2 processor and auxiliary data for ESA Version 8 final full mission analysis of MIPAS measurements on ENVISAT. Atmospheric Measurement Techniques, 2022, 15(6): 1871-1901.